analytical chemistry

pubs.acs.org/ac Article

Upconversion Luminescence-Initiated and GSH-Responsive Self-Driven DNA Motor for Automatic Operation in Living Cells and In Vivo

Cheng-Yu Li,* Jun-Xian Liu, Liu Yuheng, Jia-Ling Gao, Ya-Ling Chen, Jing-Wei He, Meng-Kun Xin, Da Liu, Bei Zheng, and Xiaoming Sun

Cite This: *Anal. Chem.* 2022, 94, 5450−5459 Read Online

ACCESS | Metrics & More | Article Recommendations | Supporting Information

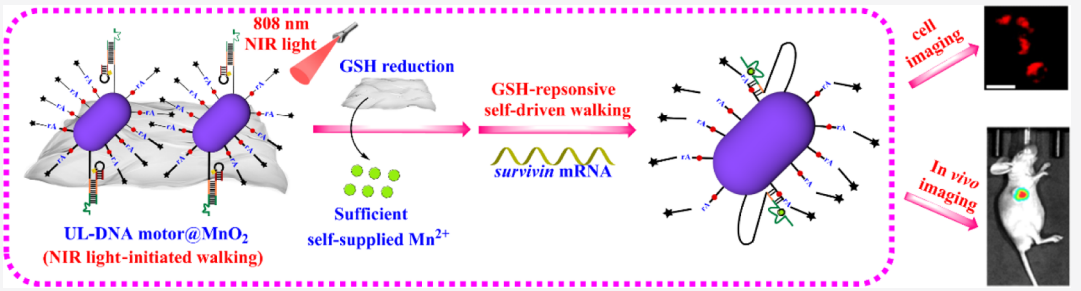

ABSTRACT: In light of the worthy design flexibility and the good signal amplification capacity, the recently developed DNA motor (especially the DNA walker)-based fluorescent biosensors can offer an admirable choice for realizing bioimaging. However, this attractive biosensing strategy not only has the disadvantage of uncontrollable initiation but also usually demands the supplement of exogenous driving forces. To handle the above obstacles, some rewarding solutions are proposed here. First, on the surface of an 808 nm near-infrared light-excited low-heat upconversion nanoparticle, a special ultraviolet upconversion luminescence-initiated three-dimensional (3D) walking behavior is performed by embedding a photocleavage linker into the sensing elements, and such light-controlled target recognition can perfectly overcome the pre-triggering of the biosensor during the biological delivery to significantly boost the sensing precision. After that, a peculiar self-driven walking pattern is constructed by employing MnO_2 nanosheets as an additional nanovector to physically absorb the sensing frame, for which the reduction of the widespread glutathione in the biological medium can bring about sufficient self-supplied Mn^{2+} to guarantee the walking efficiency. By selecting an underlying next-generation broad-spectrum cancer biomarker (*survivin* messenger RNA) as the model target, we obtain that the newly formed autonomous 3D DNA motor shows a commendable sensitivity (where the limit of detection is down to 0.51 pM) and even an outstanding specificity for distinguishing single-base mismatching. Beyond this sound assay performance, our sensing approach is capable of working as a powerful imaging platform for accurately operating in various living specimens such as cells and bodies, showing a favorable diagnostic ability for cancer care.

Thanks to the high flexibility and the favorable sensitivity, the currently proposed DNA motors-based fluorescent biosensors are more promising in detecting low-abundance biomolecules.[1−3] In general, the construction of this motor system is based on a classical Watson−Crick base pairing criterion, and a wide variety of practical concepts (e.g., tweezers,[4,5] gears,[6] wheels,[7] and walkers[8−10]) have been proposed. Of these, the DNA walkers show a better signal amplification ability by taking advantage of their efficient mechanical-like movement along a pre-set route. With the rapid development of interface materials, the previous low-dimensional walking behaviors are progressively replaced by the new three-dimensional (3D) modes to obtain higher mobile efficiency.[11] Benefiting from these merits, the application of 3D DNA walker-assisted fluorescent biosensors has been extended from the early in vitro assay to the current bioimaging. Despite much progress having been achieved, this attractive sensing option still suffers from the following challenges.

First of all, attributed to the fact that most of the detection targets are widespread in living organisms, the predetermined sensing steps will be inevitably initiated during the biological delivery.[12] Subject to this poor controllability, the final detected fluorescence information corresponding to the spatial

Received: February 20, 2022
Accepted: March 15, 2022
Published: March 24, 2022

https://doi.org/10.1021/acs.analchem.2c00830
Anal. Chem. 2022, 94, 5450−5459

Scheme 1. Construction Process of UL-DNA motor@MnO_2 (A) and Its Biological Operation Flow for Imaging *survivin* mRNA (B)

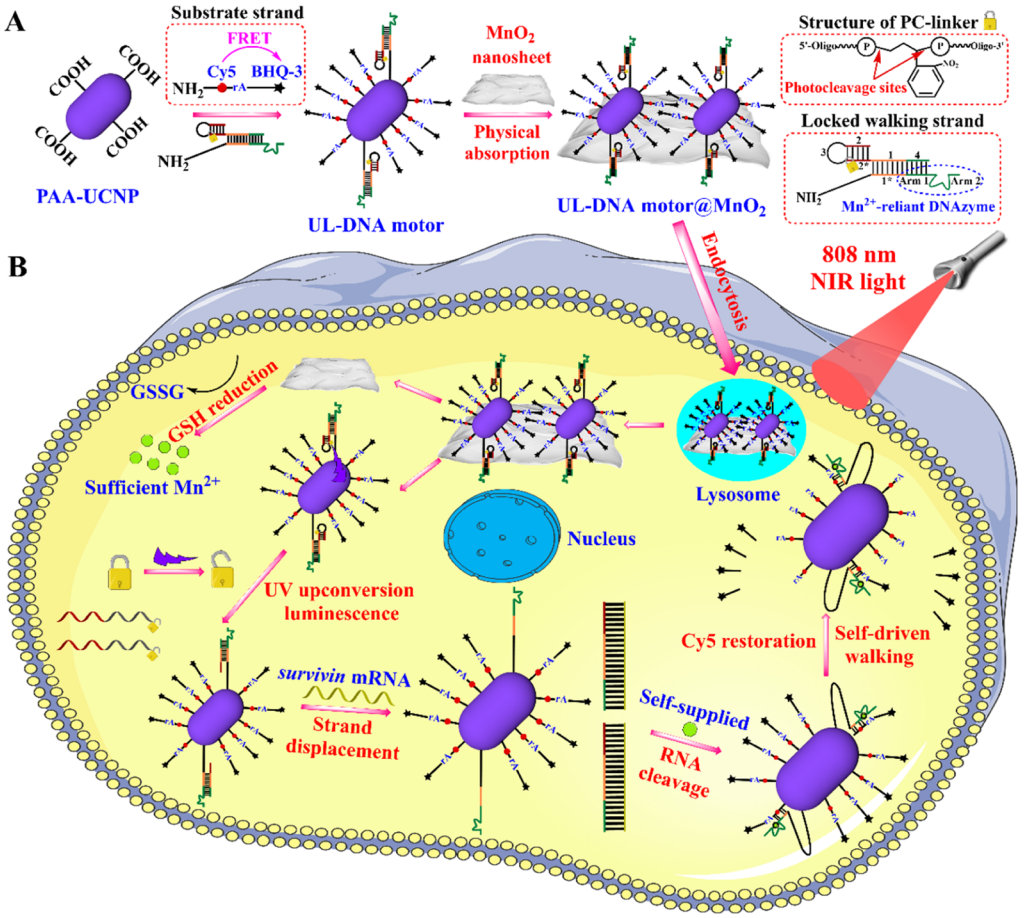

positions where the biosensors reach is hardly to uncover the true target contents. As a result, exploring a breakthrough strategy to further improve the sensing precision is of great necessity. Inspiringly, a unique photocleavage linker (PC-linker)-induced target recognition is promising in addressing this concern.[13−15] In actual operation, the *O*-nitrobenzyl-composed PC-linker[16] is embedded into a specific sensing element, and the expected PC effect is actualized via a 365 nm ultraviolet (UV) light irradiation. By integrating this processing, not only the walking behaviors are completely controllable but also the spatial/temporal imaging resolutions are notably promoted. Even so, the choice of the light source is an important factor. Compared with the obvious phototoxicity and the insufficient penetration of UV light, a special upconversion luminescence excited by a near-infrared (NIR) light is an ideal selection.[17] For the present upconversion nanoparticles (UCNPs), a type of low-heat UCNPs (rather than the frequently used 980 nm NIR light excitation) are more beneficial for performing bioimaging because of the extremely weak absorption capability of water molecules at 808 nm.[18,19] To date, the usage of such anti-Stokes UV luminescence to initiate the DNA walkers has not been reported yet.

Moreover, because the DNA walkers require plentiful driving forces to ensure an efficient surface walking behavior, there is another significant point of whether the biologically endogenous sources are capable of fulfilling this goal. Commonly, the vast majority of driving forces come from the utilization of metal ions-reliant DNAzymes, while their cofactors in the biological medium are not enough.[20] Under this unfavorable circumstance, excess metal ions are needed to be compensated to guarantee the final signal amplification. Nevertheless, the above exogenous supplementary with an uncertain manner is very likely to produce an adverse effect to the bioactivity, and it is also difficult to ensure the homogeneity of the overall concentration.[21] Therefore, it is desirable to further establish a self-driven DNA walker. Encouragingly, a sort of arresting two-dimensional nanomaterials, the MnO_2 nanosheets, is hopeful in undertaking this task.[22−25] In general, a mass of Mn^{2+} can be easily obtained when the MnO_2 nanosheets are reduced by many reductive substances (especially the high-concentration biothiols), and thus, they can serve as powerful self-supplied force sources. More than this, by means of the extensively existed $\pi-\pi$ stacking effect of two-dimensional interfaces, the entire sensing frames are able to be stably attached through a simple physical absorption for delivery into the organisms.[25]

On the grounds of these insights, we are here motivated to put forward a special 3D DNA walker by initiating using an 808 nm NIR light-excited UV upconversion luminescence and self-driving via the reduction of MnO_2 nanosheets and apply this autonomous fluorescence biosensor to implement a high-performance imaging assay in living cells and bodies. As a proof-of-concept investigation, an underlying next-generation broad-spectrum cancer biomarker, *survivin* messenger RNA (mRNA), is chosen as the model target.[26,27] The construction

https://doi.org/10.1021/acs.analchem.2c00830
Anal. Chem. 2022, 94, 5450−5459

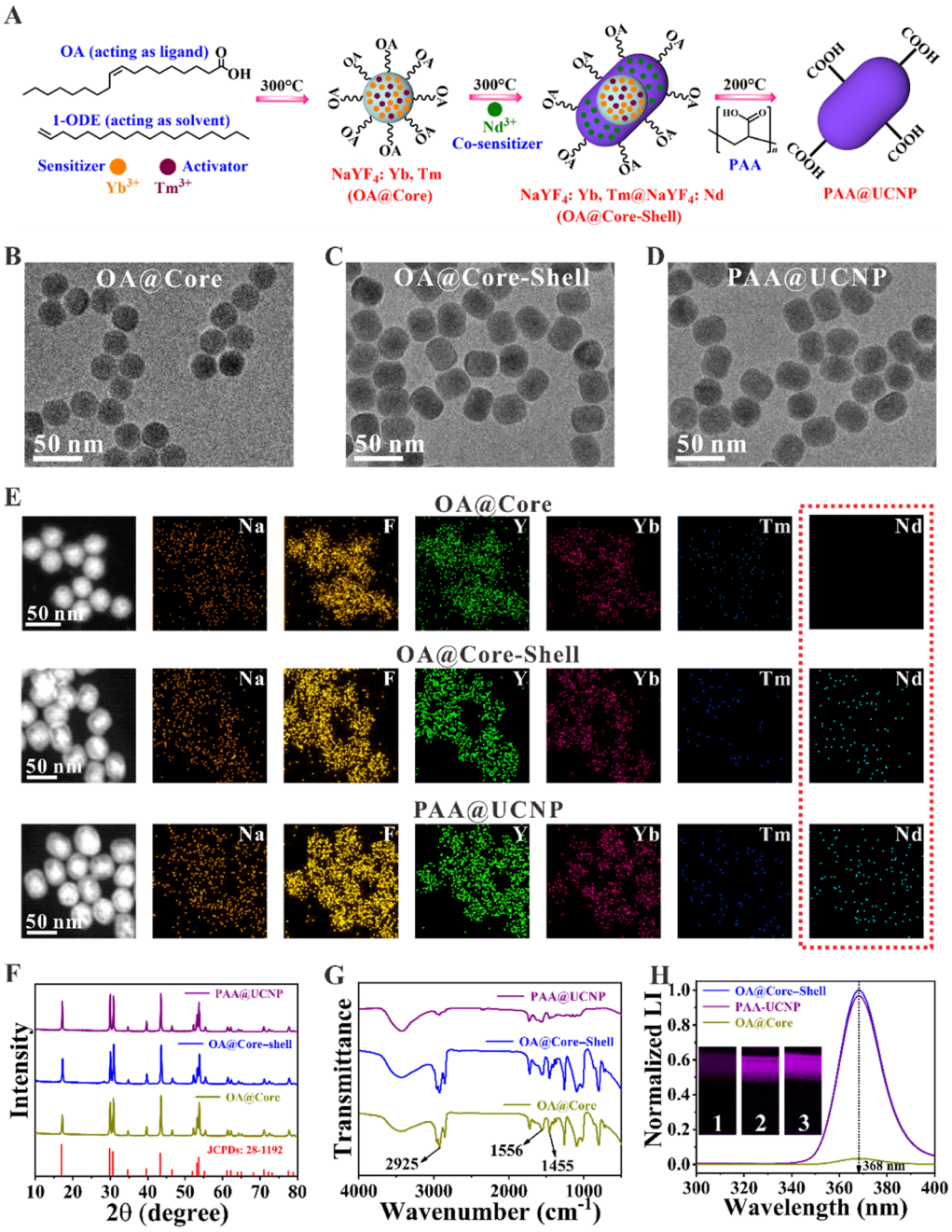

Figure 1. (A) Layer-by-layer preparation process of PAA@UCNP. (B–D) TEM images (scale bars are 50 nm) of OA@Core, OA@Core–Shell, and PAA@UCNP. (E–H) *Elemental mappings* (scale bars are 50 nm), XRD patterns, FT-IR spectra, and upconversion luminescence spectra (excited by an 808 nm NIR laser) of corresponding nanostructures. Insets in 1H: digital photos of corresponding upconversion luminescence in chloroform (1–3) and deionized water (4).

process of our sensing frame and the biological operation flow are collectively exhibited in Scheme 1. In particular, a walking strand (as long as 73 nt) containing a Mn^{2+}-reliant DNAzyme and a poly T is first treated by annealing to a PC-linker-embedded hairpin locking strand to achieve a blocking event, and then, a certain proportion of such a locked walking strand and substrate stands involved with a fluorescence resonance energy transfer (FRET) between cyanine 5 (Cy5) and black hole quencher 3 (BHQ-3) are conjointly bound onto the surface of a polyacrylic acid (PAA)-functionalized UCNP (termed as PAA@UCNP). After using a MnO_2 nanosheet to physically absorb the as-obtained motor system (termed as UL-DNA motor), the final sensing frame (termed as UL-DNA motor@MnO_2) is prepared.

When the as-fabricated nanocomposite is delivered into the cytoplasm through the endocytosis of a cellular lysosome, the UL-DNA motor is discharged from the basal plane of a MnO_2 nanosheet through the oxidation–reduction reaction of glutathione (GSH), after which sufficient Mn^{2+} ions are generated, and the GSH is switched to GSSH. Once the cell is subjected to a moderate 808 nm NIR light irradiation, the UV upconversion luminescence can render the release of the hairpin region of the locking strand from the duplex structure, and the intracellular *survivin* mRNA will result in a strand displacement to the remaining locking strand. At this time, a

https://doi.org/10.1021/acs.analchem.2c00830
Anal. Chem. 2022, 94, 5450–5459

new double strand is re-formed by reason of the hybridization between the exposed binding arms of the walking strand and part of the substrate strand. Once the loop domain of such a DNAzyme is incorporated with the self-supplied Mn^{2+}, a continuous RNA cleavage phenomenon is triggered for plenty of substrate strands to conduct the anticipated self-driven walking behavior on the 3D surface of the UCNP, and the previously quenched Cy5 emissions are finally restored.

EXPERIMENTAL SECTION

Preparation of the Oleic Acid Ligand-Stabilized UCNP (Termed as OA@Core). First, to a three-necked flask (100 mL) were added in turn 21 mL of a mixed solution [volume ratio of oleic acid (OA) and 1-octadecene (1-ODE) is 3:5] and 1 mmol lanthanide chloride hydrates in a specific proportion (Y/Yb/Tm = 0.695:0.3:0.05), followed by treatment with vacuum for 30 min under vigorous magnetic stirring. After that, the slurry was given an Ar atmosphere and heated to 150 °C. The flask was kept warm until a homogeneous solution (faint yellow) formed and then was cooled to room temperature, and to the flask, a freshly dissolved methanol solution containing NH_4F (2.5 mmol) and NaOH (4 mmol) was added dropwise. Next, an oleate intermediate in a turbid state was obtained by gently stirring the mixture for 10 min, and the internally useless solvents with low boiling points such as methanol and residual water were further evaporated by degassing the flask at 100 °C until a transparent liquid was obtained. At this time, the as-obtained reaction system was rapidly heated to 300 °C in 15 min, and such a high-temperature environment was maintained for 60 min. When the formative golden-yellow solution was cooled again, an addition of excess ethanol was performed to precipitate the white solids, and the turbid solution was divided into several repackaging tubes (5 mL). Subsequently, the products were collected by centrifuging the tubes for 5 min (12 000 rpm) and then washing four times with a water/ethanol mixture (volume ratio is 1:1) to remove the redundant inorganic and organic reagents, followed by purifying with a hexane/ethanol mixture (volume ratio is 1:3) three times. To fully disperse the nanoparticles, the as-prepared OA@Core was subjected to ultrasonic processing in 6 mL of chloroform for 3 min (concentration is 7.5 mg/mL) and finally stored in a 4 °C freezer for later use.

Development of the Shell Layer (Termed as OA@Core−shell). To a three-necked flask (50 mL) containing 3 mL of OA and 7.5 mL of 1-ODE was first added 0.72 mmol $YCl_3{\cdot}6H_2O$ and 0.08 mmol $NdCl_3{\cdot}6H_2O$, and then, the solution was treated with vacuum for 30 min. Next, the slurry was heated to 150 °C under an Ar atmosphere, and vigorous stirring was maintained for 60 min until it turned into a clear solution. After cooling to room temperature, the mixture was carefully injected with the previously prepared OA@Core drop by drop, followed by the addition of a 5 mL mixture of NH_4F (1.25 mmol) and NaOH (2 mmol) dissolved in methanol. Upon fully degassing the cloudy oleate intermediate at 100 °C to evaporate the useless chloroform and methanol, the mixture temperature was quickly increased to 300 °C, and vigorous stirring was continued for 40 min. By successively precipitating, washing, and purifying the collected products as in the previous steps, the final OA@Core−shell was treated with ultrasonic processing in 3 mL of chloroform (concentration is 15 mg/mL) for 5 min and further stored in a 4 °C freezer for later use.

PAA Functionlization of OA@Core−shell. At first, to a three-necked flask (50 mL) was added in turn 1000 mg of PAA and 20 mL of polyethylene glycol. After thoroughly mixing and treating with vacuum, the slurry was heated to 120 °C under an Ar atmosphere until a clear solution was formed. Then, the previously prepared OA@Core−Shell was injected dropwise into the flask, followed by degassing the mixture at 50 °C for 20 min. Subsequently, the flask was heated to 200 °C as quickly as possible and maintained to be warm for 90 min. Thereafter, an addition of 20 mL ethanol was performed to the formative yellow solution to precipitate the products. Next, the nanoparticles were collected via high-speed centrifugation (20 000 rpm) and further washed several times with ethanol to discard the unreacted PAA. Finally, the resulting PAA@UCNP was subjected to ultrasonic processing in 2 mL of deionized water (concentration is 10 mg/mL) and stored in a 4 °C freezer for long-term preservation.

RESULTS AND DISCUSSION

To begin with, OA@Core−Shell is prepared by employing a seed growth-based synthetic route,[28] for which thermal decomposition, which severally uses 1-ODE and lanthanide chlorides as the solvent and the precursors, respectively, is performed to create each nanostructure at 300 °C (Figure 1A). Briefly, a hydrophobic core possessing a highly efficient conversion to UV emission is first developed by co-doping the sensitizer (30% Yb^{3+}) and the activator (0.5% Tm^{3+}) into an inert $NaYF_4$ matrix (expressed as $NaYF_4$: Yb, Tm), and then, another $NaYF_4$ shell containing 10% Nd^{3+} (which acts as a co-sensitizer to effectively absorb 808 nm NIR light) is prolonged onto such a core layer (expressed as $NaYF_4$: Yb, Tm@$NaYF_4$, Nd). After that, aiming at the follow-up biomolecular coupling experiment, the as-obtained nonpolar surface is necessary to be further transformed into a water-soluble one via a facilitate liquid-to-liquid ligand replacement resulting from the stronger coordination affinity of PAA,[29] and the final PAA@UCNP is coated with abundant carboxyl groups.

The morphology evolution of such a crystal broadening event is visibly exhibited in the transmission electron microscopy (TEM) images (Figure 1B,C). Apart from the favorable dispersion, it is also found that the initial spherical core turns into a rod shape when fulfilling the shell development. Corresponding particle statistics (n = 300) uncover that fairly uniform size distributions (relative standard deviation values are at round 6%) are vested in both cases (Figures S1 and S2). Specifically, the average diameter of OA@Core is 26.64 nm, and the average length and width of OA@Core−Shell are 41.23 and 30.87 nm, respectively. Of note, no evident morphology and length−width ratio changes are observed in the ultimate hydrophilic modification (Figures 1D and S3). Elemental mappings (Figure 1E) reveal that the essential lanthanide ions (Yb^{3+} and Tm^{3+}) for realizing the anti-Stokes UV luminescence are successfully located in the core structure and the co-sensitizer (Nd^{3+}) is only presented in the formation of the shell layer. X-ray diffraction (XRD) patterns (Figure 1F) manifest that single crystal properties are endowed with all the nanostructures, and their characteristic diffraction positions faultlessly agree with the normative $NaYF_4$ in the hexagonal phase (JCPDs: 28-1192). The discovery of such lattice consistency is further demonstrated by a series of high-resolution TEM images (Figure S4), from which the adjacent plane distances of these highly crystalline domains are

https://doi.org/10.1021/acs.analchem.2c00830
Anal. Chem. 2022, 94, 5450−5459

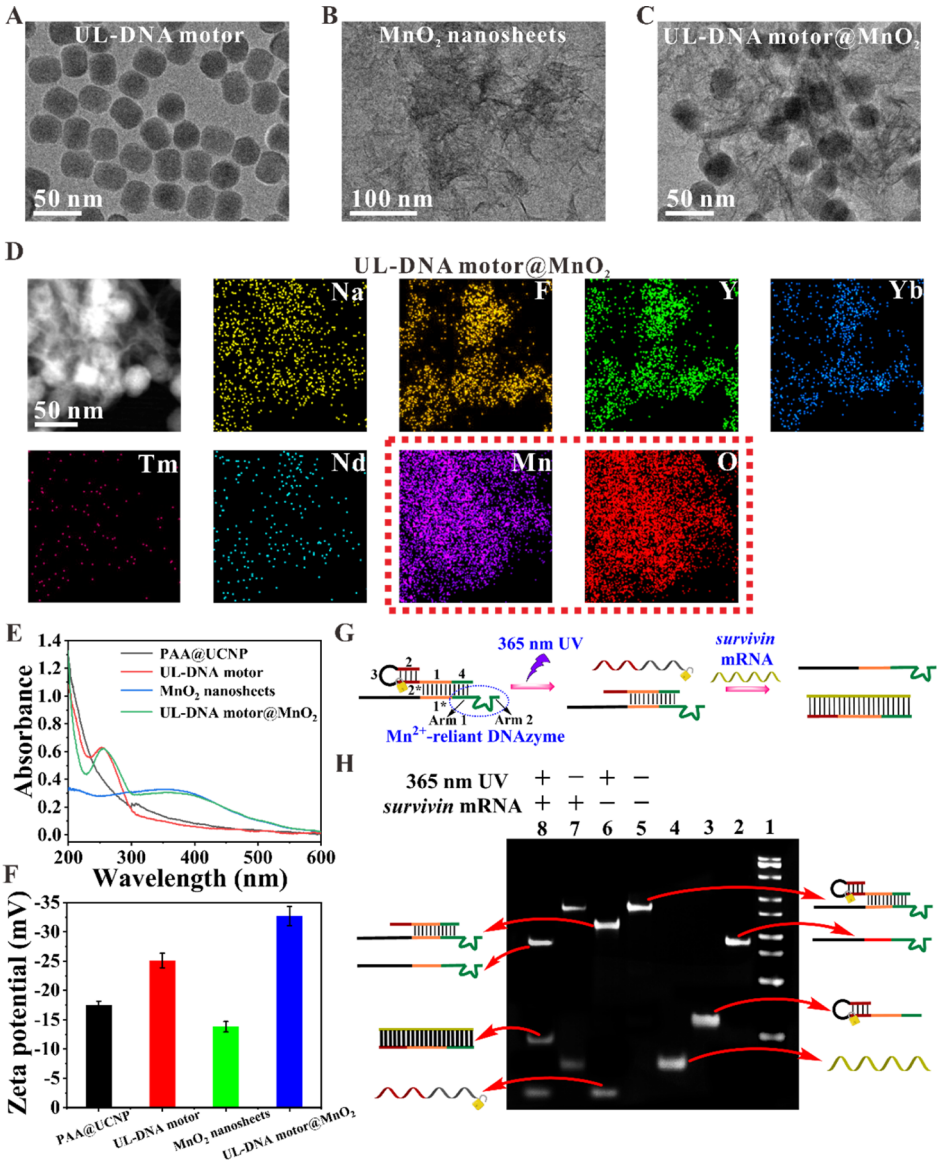

Figure 2. (A–C) TEM images of the UL-DNA motor, MnO_2 nanosheets, and UL-DNA motor@MnO_2. Scale bars are 50, 100, and 50 nm, respectively. (D) *Elemental mappings* (scale bars are 50 nm) of UL-DNA motor@MnO_2. (E) UV–visible absorption spectra of PAA@UCNP, UL-DNA motor, MnO_2 nanosheets, and UL-DNA motor@MnO_2. (F) Zeta potentials of corresponding cases in 2E. (G) Investigation principle of UV-induced strand displacement in the presence of *survivin* mRNA. (H) 6% PAGE verification of the reaction in 2G.

maintained to be ∼ 5.2 Å, suggesting the existence of a (100) crystal face of β-$NaYF_4$ during our preparation process.

Along with the presence of some featured transmittance bands, for example, the stretching of the alkyl chain at 2925 cm^{-1} and the symmetric (1556 cm^{-1}) and the antisymmetric (1455 cm^{-1}) vibrations of carboxylate anions, in the Fourier transform infrared (FT-IR) spectra (two bottom lines in Figure 1G), the surface OA loadings are confirmed to be resultful, and homogeneous solutions are formed upon dispersing these nanoparticles into chloroforms (left images in Figure S5). Upon performing the ligand replacement, the above band indications show a conspicuous weakening trend (top line in Figure 1G), and this variation will result in a commendable water solubility (right image in Figure S5). After irradiating these solutions with an 808 nm NIR laser to determine the upconversion luminescence spectra (Figure 1H), it is found that the maximal emission wavelengths for all cases are concentrated at 368 nm, which is very suitable for the photocleavage of the PC-linker. Comparatively, owing to the facts that Nd^{3+} itself has a large absorption cross-section toward 808 nm NIR light and the constructed core–shell structure can simultaneously provide an effective energy transfer pathway from Nd^{3+} to Yb^{3+} (Figure S6), the additional introduction of Nd^{3+} is capable of enhancing the UV intensity by as high as 28 times. In addition, it should be pointed out that negligible luminescence fluctuations are found to be due to the PAA functionalization.

Subsequently, the amino-modified substrate strand and locked walking strand in a definite molar proportion (10:1) are covalently coupled onto the surface of PAA@UCNP through the conventional EDC chemistry to fabricate the UL-DNA motor. Then, by making use of the van der Waals interaction, the above motor system is physically absorbed onto the MnO_2 nanosheets, which are created by oxidizing Mn^{2+} to obtain the final nanocomposites. A succession of TEM images (Figure 2A–C) manifest that the coupling of DNA

https://doi.org/10.1021/acs.analchem.2c00830
Anal. Chem. 2022, 94, 5450–5459

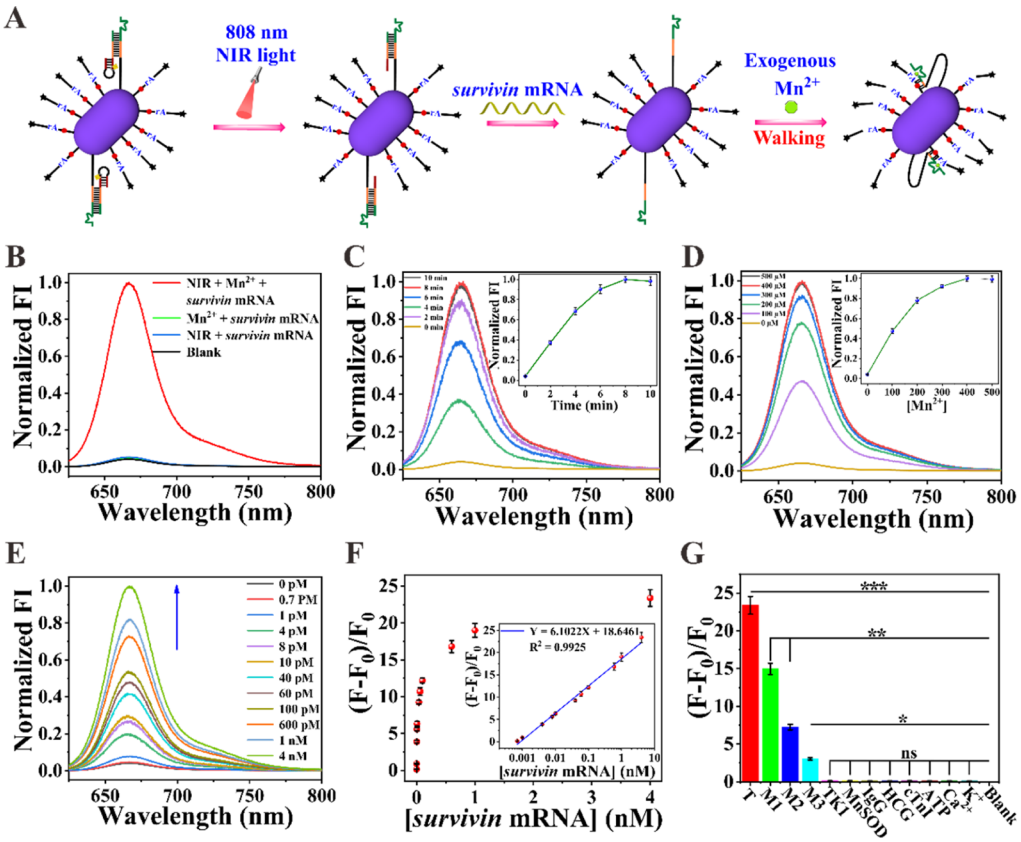

Figure 3. (A) Investigation principle of the in vitro sensing performance of the UL-DNA motor by supplementing with exogenous Mn^{2+}. (B) Sensing response of the UL-DNA motor with 808 nm NIR light irradiation, exogenous Mn^{2+}, and *survivin* mRNA. (C) Dependence of light irradiation time. (D) Dependence of $[Mn^{2+}]$. (E) Restoration of Cy5 fluorescence under the additions of different amounts of targets. (F) Linear working curve between the signal restoration rate and [*survivin* mRNA]. (G) Specificity examination for mismatching targets and other nonspecific substances. ***$P < 0.001$, **$P < 0.01$, and *$P < 0.05$, ns: no significant difference.

molecules does not influence the excellent colloidal nature (still maintaining the rod shape) of the core−shell-structured UCNPs as well as their optical quality (Figure S7), and the regularly lamellar basal planes of MnO_2 nanosheets (average sizes are ∼ 145 nm, Figure S8) can availably adhere to a number of UL-DNA motors. Such an attachment phenomenon is also certified by the elemental mappings (Figure 2D), from which obvious distributions of Mn and O elements are captured. Furthermore, UV−visible absorption spectra (Figure 2E) are exploited to prove the success of our preparation steps. To be specific, except for the distinct new peak derived from nucleic acids at 260 nm,[30] another broad absorption signal belonging to the MnO_2 matrix at 340 nm appears for UL-DNA motor@MnO_2. Not only these, both the bio-coupling and the assembly events significantly reduce the zeta potentials (Figure 2F).

In our sensing design, the recognition of *survivin* mRNA is actualized by applying the UV upconversion luminescence to touch off a strand displacement, and thus, this prerequisite is a key concern. To this end, we take advantage of a 6% polyacrylamide gel electrophoresis (PAGE) experiment to investigate the identification feasibility between the locked walking strand and the target under a 365 nm UV light induction (Figure 2G). In Figure 2H, by reason of the fact that the UV light can disconnect the linked nucleic acid strands at both terminals of the PC-linker, the irradiation case causes the hairpin region ("2 + 3" part) of the locking strand to release from the duplex structure, and the remaining double strand displays a slightly faster migration speed (lane 6). Moreover, because the target has a much stronger base pairing capacity to combine the rest of the locking strand ("2* + 1 + 4" part), the walking strand is replaced, and an additional electrophoretic strip attributing to the newly formed complementary product is finally obtained (lane 8), while the *survivin* mRNA alone cannot cause this reaction (lane 7).

Beyond this, due to the fact that our walking behavior is triggered by the continuous RNA cleavage of the metal ions-reliant DNAzyme, another issue of whether Mn^{2+} can act as a valid cofactor emerges. For this purpose, PAGE inspection is carried out again toward a facile hybridization-based FRET model (Figure S9A). After introducing this system with Mn^{2+}, it is discovered that the substrate strand is dissociated from the binding arms of the Mn^{2+}-reliant DNAzyme to result in an overt degradation (Figure S9B), illustrating that the loop domain of the DNAzyme can incorporate its cofactor well to complete the expected enzymatic reaction at the rA site. Besides, we synchronously acquire that the increase of Mn^{2+} concentration is more conductive to such a cleavage phenomenon (Figure S10A). More importantly, the DNAzyme exhibits an eminent selectivity to Mn^{2+}, and other common cations from monovalent to tervalent are unable to make a contribution to the fluorescence restoration (Figure S10B), laying a forceful guarantee for the walking accuracy.

On the basis of the aforementioned preliminary verifications, we start to evaluate the in vitro sensing performance of the UL-DNA motor by analyzing the standard *survivin* mRNA under

https://doi.org/10.1021/acs.analchem.2c00830
Anal. Chem. 2022, 94, 5450−5459

the supplement of exogenous Mn^{2+} (Figure 3A). Before this, the coexistence necessity of the initiation light (power density is low to 4.5 W/cm^2), the supplied driving forces, and the target is commendably attested by the fluorescence study (Figure 3B). More than that, it is observed that our assay system presents a remarkable irradiation time (Figure 3C) and [Mn^{2+}] (Figure 3D) dependence, where the walking behavior reaches the best efficiency when the two factors are selected to be 8 min and 400 μM, respectively.

With the assistance of the optimal temperature (37 °C, Figure S11A), pH (7.4, Figure S11B), and ion strength (100 mM NaCl, Figure S11C), we are able to obtain that the progressive introduction of *survivin* mRNA can lead to a more apparent restoration tendency to the quenched Cy5 emissions in a fairly wide target concentration range (0.7 pM to 4 nM, Figure 3E). After choosing the corresponding maximum peak point as the signal intensity to seek the operational working curve, it results in a finding that the logarithm of [survivin mRNA] being more than 4 orders of magnitude also presents an admirable linear correlation (R^2 is up to 0.9925, Figure 3F) to the signal restoration rate [denoted by $(F-F_0)/F_0$, where F is the fluorescence intensity in the presence of the target and F_0 is the blank intensity]. By means of the 3σ rule (σ signifies the standard deviation of seven parallel tests in the absence of the target) to assess the sensitivity, it is calculated that the limit of detection (LOD) for this exceptional DNA motor is as low as 0.51 pM.

In consideration of the potential homologies of mRNA members,[26] another important sensing parameter is the specificity. To examine this focus, this newly formed biosensor is further used to obtain responses for the mismatching substances with only one to three bases (indicated as M1, M2, and M3, respectively) and two mRNAs with great sequence differences (TK1 and MnSOD mRNAs). The detection data are shown in Figure 3G, among which the most arresting Cy5 restoration is assigned to the perfect target group (indicated as T). Profiting from the rigor implementation rationale of strand displacement,[31] the gradually increasing mismatches will bring about much weaker fluorescence signals. In detail, the restoration rates of M1, M2, and M3 are sharply declined to take up 64, 31, and 13% of T, respectively, and the entirely disparate mRNAs have difficulty in producing detectable intensities. Aside from this distinguishing ability for single-base variation, regarding the possibility that the extensive biomolecules in a biological medium can result in interference to the fluorescence output, some representative human proteins [immunoglobulin G, human chorionic gonadotropin, and cardiac troponin I] and small molecules (adenosine 5′-triphosphate, Ca^{2+}, and K^+) are subsequently verified. As is anticipated, these absolutely nonspecific objects cannot generate the Cy5 emissions that differ from those of the blank group.

Having explored the worthy sensing results via the artificial supplementary driving forces, the in vitro assay ability of the self-driven walking pattern is then validated by exploiting UL-DNA motor@MnO_2 (Figure S12A). In the first place, with a view to the biological GSH content (usually 1−10 mM),[32] it should be observed whether such a concentration range is sufficient for reducing the MnO_2 nanosheets to fully discharge the UL-DNA motor. Satisfactorily, the original UV−visible absorption spectrum of MnO_2 nanosheets (0.3 mg/mL) is completely disappeared when they are incubated with a very small quantify of GSH (0.8 mM, Figure S12B), and this oxidation−reduction reaction takes only about 30 s to transform the golden brown solution into a clear state (insets in Figure S12B). Likewise, the indispensable demand of GSH for launching our sensing procedures is assured (Figure S12C), and the optimum [GSH] is set to be 0.8 mM (Figure S12D).

Concurrently, on the basis of the enough self-supplied Mn^{2+}, no pronounced alternations occur in the Cy5 restoration manner spanning through 0.7 pM to 4 nM (Figure S12E), the linear operating relation (Figure S12F, whose LOD is evaluated to be 0.47 pM), and the analytical competence for differentiating single-base mismatching (Figure S12G) by comparing with the usage of the UL-DNA motor. Those findings primely account for the fact that the additional integration of such a self-driven pattern not only offers a more automatic sensing flow but also retains an outstanding sensitivity (the LOD is superior to that of other mRNA fluorescent biosensors, Table S1) and specificity to settle for the next bioimaging application.

Considering the possible cytotoxicity of the light irradiation and the nanovectors-based biological delivery, methyl thiazolyl tetrazolium assays are first applied to test the cellular growing state of two cancer cells (HeLa and MCF-7) and one normal cell (L02). As expected, thanks to the extremely weak absorption of water molecules at 808 nm, we can discover that the cell viabilities of this group are notably better than those of groups treated with 980 nm NIR light and 365 nm UV light under the same power density and irradiation time (Figure S13A). Other than this, ascribing to the merit of non-heavy-metal elements in our nanocomposites, the percentages of living cells for all cases are capable of being sustained to ∼90% even if the incubation concentrations reach up to 1 mg/mL (Figure S13B). Furthermore, the endocytic pathway of UL-DNA motor@MnO_2 is ascertained via lysosomal co-location tracking (Figure S14), where an accurate signal overlapping with the Cy5 emissions provides direct evidence that a lysosome resultant endocytosis renders the eventual delivery of our biosensor to the cytoplasm.

According to the postoptimized intracellular imaging conditions, where the nanocomposite concentration and the incubation time are chosen to be 0.3 mg/mL (Figure S15) and 3 h (Figure S16), respectively, the living cell application for the above cancer and normal cell lines is carried out. As we suspected, the UL-DNA motor@MnO_2-supported biosensor is in an absolute silence state when the cells are not treated with the 808 nm NIR light irradiation, and their Cy5 fluorescence is hardly to be captured (top images in Figure 4A−C). In stark contrast to the unresponsive events, the initiated biosensor (performing the light treatment) produces overt signal intensities stemming from the DNA motor system-caused fluorescence restoration (bottom images in Figure 4A−C), revealing a good working adaptation in a cellular medium. Further image quantification of gray levels using conventional ImageJ software reveals that the mean Cy5 brightness of these light-irradiated cells is successively ∼ 6.51-fold (HeLa), ∼ 5.05-fold (MCF-7), and ∼ 2.24-fold (L02) higher than that in the corresponding unactivated cases (Figure 4D) and that of the HeLa group is found to be about 1.46 times that of the MCF-7 group. We speculate that the above statistical discrepancy is put down to the overexpression feature of *survivin* mRNA in various cancer-associated cells.[26] Meanwhile, an insignificant distinction between the imaging results and the flow cytometry determinations is demonstrated (Figure 4E), and such a target content tendency is also validated by the

https://doi.org/10.1021/acs.analchem.2c00830
Anal. Chem. 2022, 94, 5450−5459

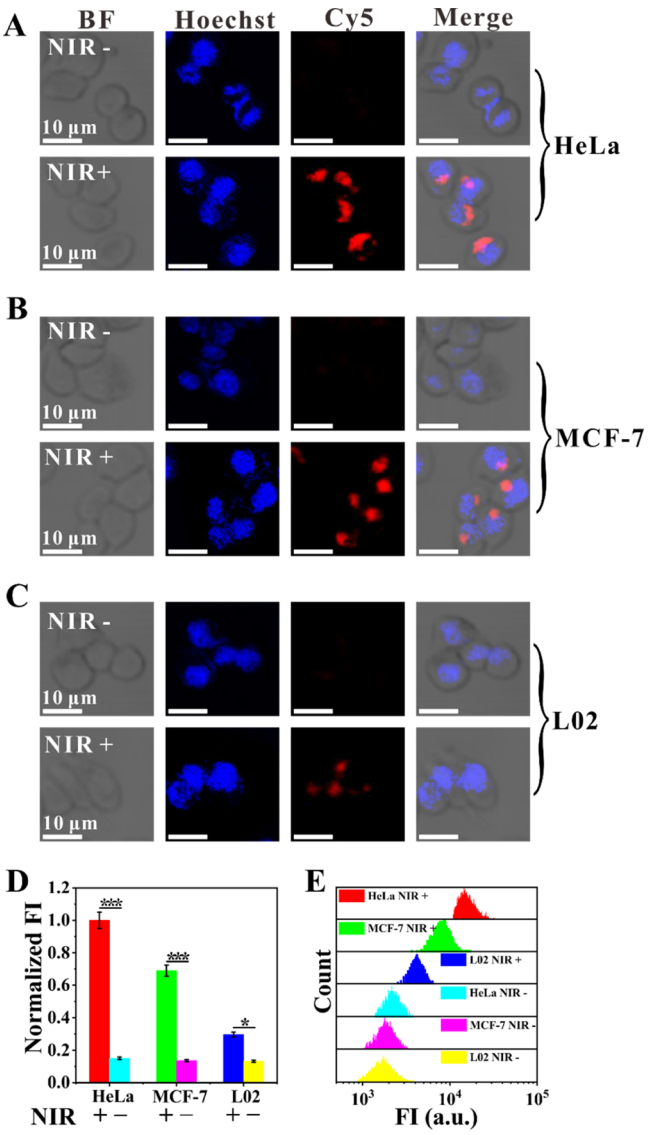

Figure 4. (A–C) Confocal images (scale bars are 10 μm) of UL-DNA motor@MnO_2-incubated HeLa, MCF-7, and L02 cells with (bottom) and without (top) the treatment of 808 nm NIR light irradiation. Fluorescence collection channel and exposure time are set to be 670 ± 50 and 250 ms, respectively. (D) Intensity quantification data of corresponding confocal images. ***P < 0.001 and *P < 0.05. (E) Flow cytometry determinations of corresponding digested cell lines. The fluorescence collection channel is set to be 670 ± 30 nm, and 10000 cells are detected for each case.

measurements of the quantitative polymerase chain reaction (qPCR, Figure S17). In summary, our fluorescent biosensor is capable of serving as a powerful imaging platform for responding the targets in a wide range of human source cells.

As a sort of next-generation cancer biomarker, *survivin* mRNA can offer potential diagnostic information for cancer care, and thus, exploring an efficient analytical approach to accomplish a monitoring task at the cellular level is of great necessity.[27] To this aim, two groups of HeLa cells are treated in turn with different concentrations of the *survivin* inhibitor [sepantronium bromide (YM155)][33] to realize a target downregulation phenomenon. In comparison to the untreated cells (top images in Figure S18A), the incremental additions of YM155 give rise to a dramatically decreased Cy5 fluorescence (middle and bottom images in Figure S18A), and such a finding can be explained by the fact that the reduced *survivin* mRNA lessens the walking frequency. Following the same quantitative steps, the signal intensities of these two biological-reagent-regulated cases are dropped to occupy ~ 66% (3 nM YM155) and ~ 39% (5 nM YM155) to that of the control group (Figure S18B), respectively. Beyond that, flow cytometry analysis is exploited to finely prove that the weakened Cy5 restorations (Figure S18C) and the intracellular target changes in different physiological states remain well-consistent with the qPCR data (Figure S19). Together, our assay method can additionally be applied as an effectual monitoring toolbox.

To our knowledge, most of the DNA motors-based fluorescent biosensors still focus on the intracellular operation, and the application of living bodies has rarely been reported. Finally, we attempt to study the imaging ability of UL-DNA motor@MnO_2 in a female BALB/c nude mouse model bearing HeLa xenograft tumor. In order to guarantee the consistency of biological subjects, the bodies weights and the tumor sizes should be kept at ~ 18 g and ~ 200 mm^3, respectively. At first, the tumor implantation areas are injected with the same concentrations (0.3 mg/mL) of UL-DNA motor@MnO_2. Then, the mice are divided into two groups, and one of their tumor locations is treated with the 808 nm NIR light irradiation for 8 min (five independent mice were detected for each group). By continuously collecting the whole body images at different time points after the injection (Figure 5), it is found that an efficient intratumoral fluorescence distribution is endowed on the nanocomposites, along with an observation that the Cy5 emissions become more and more apparent with the time evolution (from 0.5 to 2 h, bottom images). Counter to this increasing sign, the fluorescence signals are almost unchanged in this time interval without the employment of the light initiation (top images), implying that our biosensor is out of operation in the unitary presence of *survivin* mRNA. Subsequent quantitative analysis reflects that the Cy5 intensities at 1 and 2 h are ~ 4.3 times and ~5.6 times higher than that of the corresponding unirradiated mice, respectively, suggesting an outstanding in vivo imaging performance.

CONCLUSIONS

In this work, an innovative 3D DNA walker-based fluorescent biosensor has been successfully developed. For one thing, a PC-linker is embedded into the locked walking strand, and the target recognition is able to be precisely actualized by treating with a UV upconversion luminescence resulting from a moderate 808 nm NIR light irradiation. For another, the wide interfaces of MnO_2 nanosheets are physically absorbed with the motor system, and the sensing frame can be efficiently discharged by adopting a facilitate GSH responsive pattern to achieve a self-driven walking behavior on the surface of the UCNP. On the basis of such attempts, a satisfactory sensing performance toward *survivin* mRNA (acted as the model target) is attributed to this new assay method, wherein the sensitivities are enhanced to sub-picomolar levels with and without the introduction of the self-driven strategy, together with a specificity for identifying single-base change. More importantly, this significantly improved DNA motor can be applied to effectively image the targets in various living biological samples (e.g., cells and bodies) at a high accuracy, for which the determination results fit nicely with the analysis

https://doi.org/10.1021/acs.analchem.2c00830
Anal. Chem. 2022, 94, 5450–5459

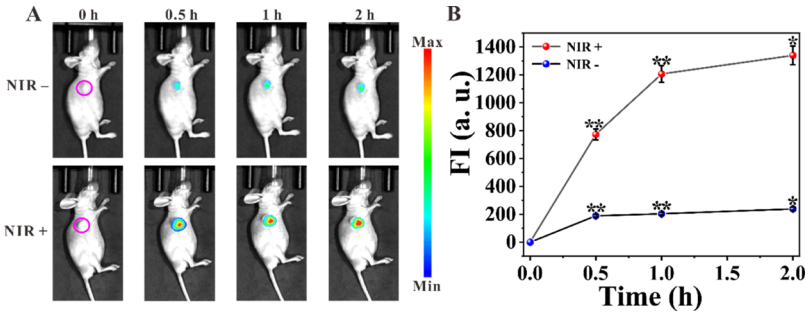

Figure 5. (A) In vivo fluorescence images of UL-DNA motor@MnO_2 with (bottom) and without (top) the treatment of 808 nm NIR light irradiation at the implantation areas (purple circles) at different time points after the injection. Five independent mice are detected for each group. Fluorescence excitation and collection channels are set to be 650 and 690 ± 25 nm, respectively. (B) Intensity quantification data of corresponding in vivo fluorescence images. $^{**}P < 0.01$ and $^{*}P < 0.05$.

of flow cytometry and qPCR, demonstrating an admirable application prospect for cancer diagnosis.

■ ASSOCIATED CONTENT

Supporting Information

The Supporting Information is available free of charge at https://pubs.acs.org/doi/10.1021/acs.analchem.2c00830.

Chemical materials and reagents, instruments, preparation of the UL-DNA motor, preparation of MnO_2 nanosheets, preparation of UL-DNA@MnO_2, in vitro detection, specificity examination, cell culture, inspection of cell viability, intracellular imaging, in vivo imaging, size distribution, high-resolution TEM images, digital photos, additional upconversion spectra, 10% PAGE analysis, sensing performance of UL-DNA@MnO_2, sensitivity comparison, optimal intracellular imaging conditions, qPCR analysis, and monitoring of intracellular *survivin* mRNA (PDF)

■ AUTHOR INFORMATION

Corresponding Author

Cheng-Yu Li − *Hubei Province Key Laboratory of Occupational Hazard Identification and Control, School of Public Health, Medical College, Wuhan University of Science and Technology, Wuhan 430065, People's Republic of China*; orcid.org/0000-0003-4463-717X; Email: lichengyu@wust.edu.cn

Authors

Jun-Xian Liu − *Hubei Province Key Laboratory of Occupational Hazard Identification and Control, School of Public Health, Medical College, Wuhan University of Science and Technology, Wuhan 430065, People's Republic of China*

Liu Yuheng − *Hubei Province Key Laboratory of Occupational Hazard Identification and Control, School of Public Health, Medical College, Wuhan University of Science and Technology, Wuhan 430065, People's Republic of China*

Jia-Ling Gao − *Hubei Province Key Laboratory of Occupational Hazard Identification and Control, School of Public Health, Medical College, Wuhan University of Science and Technology, Wuhan 430065, People's Republic of China*

Ya-Ling Chen − *Hubei Province Key Laboratory of Occupational Hazard Identification and Control, School of Public Health, Medical College, Wuhan University of Science and Technology, Wuhan 430065, People's Republic of China*

Jing-Wei He − *Hubei Province Key Laboratory of Occupational Hazard Identification and Control, School of Public Health, Medical College, Wuhan University of Science and Technology, Wuhan 430065, People's Republic of China*

Meng-Kun Xin − *Hubei Province Key Laboratory of Occupational Hazard Identification and Control, School of Public Health, Medical College, Wuhan University of Science and Technology, Wuhan 430065, People's Republic of China*

Da Liu − *College of Chemistry and Molecular Sciences, Wuhan University, Wuhan 430072, People's Republic of China*

Bei Zheng − *Westlake Institute for Advanced Study, School of Life Sciences, Westlake University, Hangzhou 310024, People's Republic of China*

Xiaoming Sun − *Hubei Key Laboratory of Embryonic Stem Cell Research, School of Basic Medical Sciences, Hubei University of Medicine, Shiyan 442000, People's Republic of China*; orcid.org/0000-0002-9546-6764

Complete contact information is available at: https://pubs.acs.org/10.1021/acs.analchem.2c00830

Notes

The authors declare no competing financial interest.

■ ACKNOWLEDGMENTS

This work was supported by the National Natural Science Foundation of China (21904102 and 81802053).

■ REFERENCES

(1) Chen, J.; Luo, Z.; Sun, C.; Huang, Z.; Zhou, C.; Yin, S.; Duan, Y.; Li, Y. *TrAC, Trends Anal. Chem.* **2019**, *120*, 115626.

(2) Zhou, B.; Dong, Y.; Liu, D. *ACS Appl. Bio Mater.* **2021**, *4*, 2251−2261.

(3) Xu, M.; Tang, D. *Anal. Chim. Acta* **2021**, *1171*, 338523.

(4) Yang, W.; Shen, Y.; Zhang, D.; Li, C.; Yuan, R.; Xu, W. *Anal. Chem.* **2019**, *91*, 7782−7789.

(5) Li, J.; Wang, W.; Zhang, H.; Lu, Z.; Wu, W.; Shu, M.; Han, H. *Anal. Chem.* **2020**, *92*, 4900−4907.

(6) Liu, X.; Zhang, J.; Fadeev, M.; Li, Z.; Wulf, V.; Tian, H.; Willner, I. *Chem. Sci.* **2019**, *10*, 1008−1016.

(7) Yang, F.; Cheng, Y.; Cao, Y.; Zhang, Y.; Dong, H.; Lu, H.; Zhang, X. *Anal. Chem.* **2019**, *91*, 9828−9835.

(8) Gao, J.-L.; Liu, Y.-H.; Zheng, B.; Liu, J.-X.; Fang, W.-K.; Liu, D.; Sun, X.-M.; Tang, H.-W.; Li, C.-Y. *ACS Appl. Mater. Interfaces* **2021**, *13*, 31485−31494.

(9) Yin, Y.; Chen, G.; Gong, L.; Ge, K.; Pan, W.; Li, N.; Machuki, J. O. a.; Yu, Y.; Geng, D.; Dong, H.; Gao, F. *Anal. Chem.* **2020**, *92*, 9247−9256.

(10) Liu, X.; Meng, F.; Sun, R.; Wang, K.; Yu, Z.; Miao, P. *Chem. Commun.* **2021**, *57*, 2629−2632.

(11) Hu, H.; Zhou, F.; Wang, B.; Chang, X.; Dai, T.; Tian, R.; Wan, Y.; Wang, X.; Wang, G. *Nanoscale* **2021**, *13*, 1863−1868.
(12) Chu, H.; Zhao, J.; Mi, Y.; Zhao, Y.; Li, L. *Angew. Chem., Int. Ed.* **2019**, *58*, 14877−14881.
(13) Zhao, J.; Chu, H.; Zhao, Y.; Lu, Y.; Li, L. *J. Am. Chem. Soc.* **2019**, *141*, 7056−7062.
(14) Zhao, J.; Li, Z.; Shao, Y.; Hu, W.; Li, L. *Angew. Chem., Int. Ed.* **2021**, *60*, 17937−17941.
(15) Gao, J.-L.; Yuheng, L.; Liu, J.-X.; Tang, H.-W.; Li, C.-Y. *Anal. Chem.* **2021**, *93*, 16638−16645.
(16) Lubbe, A. S.; Szymanski, W.; Feringa, B. L. *Chem. Soc. Rev.* **2017**, *46*, 1052−1079.
(17) Li, C.-Y.; Zheng, B.; Kang, Y.-F.; Tang, H.-W.; Pang, D.-W. *ACS Sens.* **2020**, *5*, 199−207.
(18) Guo, S.; Tsang, M.-K.; Lo, W.-S.; Hao, J.; Wong, W.-T. *Nanoscale* **2018**, *10*, 2790−2803.
(19) Chan, M.-H.; Chen, S.-P.; Chen, C.-W.; Chan, Y.-C.; Lin, R. J.; Tsai, D. P.; Hsiao, M.; Chung, R.-J.; Chen, X.; Liu, R.-S. *J. Phys. Chem. C* **2018**, *122*, 2402−2412.
(20) Liu, J.; Cui, M.; Zhou, H.; Yang, W. *ACS Sens.* **2017**, *2*, 1847−1853.
(21) Ma, P.-Q.; Liang, C.-P.; Zhang, H.-H.; Yin, B.-C.; Ye, B.-C. *Chem. Sci.* **2018**, *9*, 3299−3304.
(22) Fan, H.; Zhao, Z.; Yan, G.; Zhang, X.; Yang, C.; Meng, H.; Chen, Z.; Liu, H.; Tan, W. *Angew. Chem., Int. Ed.* **2015**, *54*, 4801−4805.
(23) Ou, M.; Huang, J.; Yang, X.; Quan, K.; Yang, Y.; Xie, N.; Wang, K. *Chem. Sci.* **2017**, *8*, 668−673.
(24) Zhang, Y.; Jiao, J.; Wei, Y.; Wang, D.; Yang, C.; Xu, Z. *Anal. Chem.* **2020**, *92*, 15244−15252.
(25) Li, Y.; Zhang, L.; Zhang, Z.; Liu, Y.; Chen, J.; Liu, J.; Du, P.; Guo, H.; Lu, X. *Anal. Chem.* **2021**, *93*, 9621−9627.
(26) Qian, G.-S.; Kang, B.; Zhang, Z.-L.; Li, X.-L.; Zhao, W.; Xu, J.-J.; Chen, H.-Y. *Chem. Commun.* **2016**, *52*, 11052−11055.
(27) Ratajczak, K.; Krazinski, B. E.; Kowalczyk, A. E.; Dworakowska, B.; Jakiela, S.; Stobiecka, M. *ACS Appl. Mater. Interfaces* **2018**, *10*, 17028−17039.
(28) Li, C.-Y.; Zheng, B.; Li, J.-T.; Gao, J.-l.; Liu, Y.-H.; Pang, D.-W.; Tang, H.-W. *ACS Nano* **2021**, *15*, 8142−8154.
(29) Li, C.-Y.; Kang, Y.-F.; Qi, C.-B.; Zheng, B.; Zheng, M.-Q.; Song, C.-Y.; Guo, Z.-Z.; Lin, Y.; Pang, D.-W.; Tang, H.-W. *Anal. Chem.* **2019**, *91*, 7950−7957.
(30) Gabelica, V.; Rosu, F.; Tabarin, T.; Kinet, C.; Antoine, R.; Broyer, M.; De Pauw, E.; Dugourd, P. *J. Am. Chem. Soc.* **2007**, *129*, 4706−4713.
(31) Simmel, F. C.; Yurke, B.; Singh, H. R. *Chem. Rev.* **2019**, *119*, 6326−6369.
(32) Lin, L.-S.; Song, J.; Song, L.; Ke, K.; Liu, Y.; Zhou, Z.; Shen, Z.; Li, J.; Yang, Z.; Tang, W.; Niu, G.; Yang, H.-H.; Chen, X. *Angew. Chem., Int. Ed.* **2018**, *57*, 4902−4906.
(33) Miyao, T.; Koike, H.; Sekine, Y.; Ohtsu, A.; Oka, D.; Suzuki, K. *Anticancer Res.* **2020**, *40*, 5091−5095.

https://doi.org/10.1021/acs.analchem.2c00830
Anal. Chem. 2022, 94, 5450−5459